Physical weathering of carbonate host-rock by precipitation of soluble salts in caves: a case study in El Orón-Arco Cave (Region of Murcia, SE Spain)

Fernando Gázquez[(1)*], José-María Calaforra[(1)], Nicholas P. Evans[(2)], Alexandra V. Turchyn[(2)], Fernando Rull[(3)], Jesús Medina[(3)], Andrés Ros[(4)], José Luis Llamusí[(4)], Juan Sánchez[(4)] and David A. Hodell[(2)]

(1) Department of Biology and Geology, Universidad de Almería, Carretera de Sacramento s.n, La Cañada de San Urbano, Almería, 04120, Spain.

(2) Department of Earth Sciences, University of Cambridge, Downing Street, Cambridge, CB2 3EQ, United Kingdom.

(3) Departamento de Física de la Materia Condensada, Cristalografía y Mineralogía. Universidad de Valladolid. Paseo de Belén, 7, 47011, Valladolid, Spain

(4) Centro de Estudios Ambientales y del Mar. CENM-naturaleza, Alcántara, 5, Cartagena, Murcia, 30394, Spain.

*corresponding author (f.gazquez@ual.es)

ABSTRACT

The dissolution of carbonate host-rock by freshwater in phreatic or vadose conditions is the most common mechanism for the formation of caves; however, circulation of saline solutions through carbonate materials and precipitation of soluble salts may also play an important role. We studied the stable isotope composition ($\delta^{18}O$ and $\delta^{34}S$ of sulfate, $\delta^{18}O$ and δD of structurally-bound gypsum hydration water and $^{87}Sr/^{86}Sr$) and salinity of fluid inclusions in gypsum speleothems found in El Orón-Arco Cave (Cartagena, SE Spain). We suggest that physical weathering of carbonate host-rock was driven by precipitation of soluble sea-salts (mostly gypsum and halite), and this process controlled the recent geomorphological evolution of the cave. The Triassic carbonate host-rock shows clear evidence for salt weathering, including gypsum/halite infillings in

cracks of the bedrock, mechanical spalling of the carbonate, and detachment of rock fragments that lead to the formation cave voids and in-situ accumulations of piles of unsorted rubble. Sulfur and oxygen isotopes of gypsum sulfate (3.0‰<δ^{18}O<11.6‰ and 16.7‰<δ^{34}S<20.7‰) are generally lower than modern seawater sulfate and suggest contributions from a ^{34}S-depleted source (i.e. oxidation of pyrite). The δ^{18}O and δD of gypsum hydration water are relatively low compared to expected values for the evaporation of pure seawater to gypsum saturation, suggesting that gypsum precipitation involved a secondary calcium-sulfate source or recycling of gypsum from previous stages, along with mixing of seawater and meteoric water seepage to the cave. The ^{87}Sr/^{86}Sr in gypsum shows intermediate values between modern seawater and Triassic carbonate values because of interaction between the solution and the bedrock. The salinities of the speleothem-forming solutions are relatively high (13.2±3.2 wt. % eq. NaCl) compared to gypsum formed from evaporated brackish solutions (i.e. ~4-8 wt. % eq. NaCl) and indicate dissolution of earlier evaporites before secondary gypsum precipitation. This cave-forming mechanism, which is related to saline water circulation and precipitation of evaporitic minerals, may be common in other coastal caves.

KEYWORDS: coastal caves, evaporites, gypsum, halite, salt weathering, gypsum speleothems, stable isotopes.

1. Introduction

The mechanisms involved in the formation of caves (i.e. speleogenesis) are generally linked to dissolution of carbonate host-rock by freshwaters undersaturated in calcium carbonate (see Audra and Palmer, 2015 for a recent review). These karstification processes create voids in the rock that can result in the breakdown and collapse of cave ceilings, eventually leading to the formation of large chambers and passages (Ginés and Ginés, 2007).

In the case of coastal caves, the dissolution of the carbonate host-rock can be enhanced by the mixing of freshwater and seawater that generates solutions undersaturated in calcite ($CaCO_3$) and dolomite ($CaMg(CO_3)_2$). These undersaturated solutions are capable of dissolving limestone and dolostones, accelerating cave forming processes (Mylroie and Mylroie, 2007). In addition to karstification processes, speleogenesis in coastal caves can be driven by the geomorphological evolution of the shoreline, in many cases connected to coastal erosion that causes landslides and fracturing (Moore, 1954). Caves that develop in coastal fractures (e.g. ‘flank margin caves’) display distinctive features compared to caves formed by dissolution (Mylroie and Carew 1990) and lack specific features generated by a subterranean water course or phreatic conduits, such as ‘scallops’ and smoothed surfaces (Mylroie and Mylroie, 2007). Additional geochemical processes in coastal karstic aquifers can also result in the formation of subterranean voids; potential mechanisms include mechanical weathering caused by the pressure generated in pores of the carbonate host-rock because of the precipitation of soluble salts (i.e. ‘gypsum/halite wedging’; White and White,

2003). However, the relative importance of salt weathering processes in coastal cave environments remains uninvestigated.

Salt weathering is known to influence the development of many geomorphologic features in different environments, including honeycombs and alveoles (Mustoe, 1982), tafoni, and cave genesis in granitic rocks (Bradley et al., 1978). Furthermore, this mechanism is an important contributor to rock debris generation in arid regions (Beaumont, 1968; Goudie and Day, 1980), coastal environments (Mottershead, 1989), and cold settings (Prebble, 1967). In this study, we examine the mineralogy and geochemistry of secondary evaporite deposits in El Orón-Arco Cave of Cabo Tiñoso ('Scabby Cape', Cartagena, Region of Murcia, SE Spain) in order to evaluate the role of sea salt weathering during its formation. Oxygen and sulfur isotopes of sulfate in gypsum ($CaSO_4 \cdot 2H_2O$) are utilized to determine the sources of sulfate for the formation of the gypsum speleothems. Oxygen and hydrogen isotopes in structurally-bonded gypsum hydration water (GHW) and salinity of fluid inclusions (i.e. microthermometry of fluid inclusions) are used to identify the source of water (seawater vs meteoric seepage; e.g. Evans et al., 2015), the degree of evaporation of the solution in the cave, and potential recycling of older evaporites before the precipitation of the gypsum speleothems. Strontium isotopes in gypsum and soluble salts in pores of the host-rock are used as an indicator of the degree of contribution of cations (calcium and strontium) from the cave matrix to the solution before gypsum precipitation. We generate a model to explain the cave formation based on geomorphological and geochemical observations, with potential implications for the genesis of other coastal caves.

2. Geological setting and cave description

El Orón-Arco Cave system is located in the southern flank of Cabo Tiñoso in Cartagena, Murcia Region, SE Spain (Fig. 1). The cavity consists of a subterranean network that extends over 1500 m, from El Arco Cave in the south-east, first surveyed in the 1980s (Llamusí et al., 1990), to the more recently discovered El Orón Cave in the north-west (Puch, 1998). El Arco Cave is also known as the 'Cave of the Great Lake' because of the presence of a 1200 m^2 brackish lake with a maximum depth of 2 m. The largest cave chamber is the 'Hall of the Chandeliers', which is located between 40 and 170 m a.s.l., representing the highest point in the cave above sea level. The rest of the passages and chambers lie between the sea level and ~40 m a.s.l. There are two entrance locations to El Orón-Arco Cave; the first is via a submarine access point (2 m b.s.l.), whereas the second consists of a subaerial entrance in the cliff of Cabo Tiñoso (~10 m a.s.l.) (Fig. 1).

The cave has formed along a fracture running NW to SE, parallel to the shoreline, in the highly foliated Triassic limestone and dolostone of the Alpujarride Formation of Cabo Tiñoso (García-Tortosa et al., 2000). A series of greyish limestones and interbedded reddish dolostones outcrop both in the cave (Fig. 2A) and outside (Fig. 2B). No evidence for phreatic dissolution or signs of subterranean runoff are found in the cave, whereas two brackish-water lakes at sea-level are the only known waterbodies at present.

Climate in this region is semi-arid, with mean annual temperature around 20 °C, maximum temperatures in August (~28 °C) and minimum in January (~14 °C). Average annual precipitation rarely exceeds 250 mm in this region and is one of the driest areas of the Iberian Peninsula. Vegetation over the cave consists of thermo-Mediterranean pre-desertic scrubs and xerophilic herbs.

3. Methods

3.1. Sampling of speleothems

We performed a detailed photographic study of the geomorphological and speleothemic features of El Orón-Arco Cave (Figs. 2 and 3) and collected 27 mineral samples for mineralogical and stable isotopes analyses (Fig. 1 for sampling site locations; Figs. 2 and 3 and Table 1 for sample descriptions). In general, sample amounts were smaller than 5 g and were preferentially selected from discreet parts of the chambers to minimize the impact on the cave environment.

Saline concretions on the cave walls were sampled from foliation planes of the host-rock in different sectors of the cave (n=8) (Figs. 2A and 3). We took samples of the foliated greyish and reddish materials that comprise the host-rock inside and outside the cave (n=4) (Fig. 2B), and one sample of yellowish calcschists from outside of the cave entrance. A sample of yellowish unconsolidated, sandy material was taken from a fracture following the foliation of the greyish host-rock in the Hall of the Chandeliers. In the same chamber, a sample of the whitish microcrystalline crust that occurs all over the ceiling in this location was collected (Fig. 3E). Another sample comprises a ~5 cm fragment from a ~1 m long

transparent euhedral crystal that hangs from the cave ceiling, resembling a 'chandelier' (Fig. 3E), and morphologically similar to those described in Lechuguilla Cave, New Mexico, USA (Davis, 2000). In places, the apices of these crystals display a ~10 cm long and 1 cm wide hollow cylinder, resembling a soda-straw, made of a transparent microcrystalline mineral (Fig. 3F). In the 'Hall of the Eccentrics', we took a ~5 g fragment of a hollow gypsum hemisphere, ~20 cm in diameter from the cave ceiling (called 'blisters' hereafter), which are surrounded by (but generally not in contact with) carbonate speleothems (Fig. 3H). Similar 'blister' speleothems have been described in Cupp-Coutunn Cave, Turkmenistan (Maltsev and Self, 1992). Lastly, a transparent single crystal was collected from the tip of a stalactite (Fig 3I). Samples (~250 mg) were ground to a fine powder and dried at 45 °C overnight for mineralogical and isotopic analyses.

3.2. Mineralogical analyses

A transmission X-ray diffraction (XRD) instrument (Terra), inXitu, Inc. (California), was utilized to determine the mineralogy of 27 samples (Sarrazin et al., 2005) at the Unidad Asociada al Centro de Astrobiologia CAB-CSIC-UVa of Valladolid University (Valladolid, Spain). Powdered samples were initially transferred into a vibrating cell. A micro-focused X-ray source (Co) (10 W) was combined with miniature slits to produce a low divergence beam illuminating the sample at a 10° incidence angle. A custom CCD camera (Andor™) was used to collect the XRD signal over a range of 5-55° of 2θ. X-ray diffractogram resolution was 0.3° of the 2θ angle. Sections of diffraction rings were collected in 2D images, while the 1D XRD patterns were calculated by circumferential integration of the diffracted intensities along diffraction rings. Diffractograms were processed by the X-

Powder software (Martín, 2004) and mineralogical determination used the PDF-2 (Power Diffraction Files) database.

3.3. Stable isotope analyses

3.3.1. Sulfur ($\delta^{34}S$) and oxygen ($\delta^{18}O_{SO4}$) in sulfate

The sulfur and oxygen isotopes of the sulfate of 13 samples were analyzed in the Godwin Laboratory at the University of Cambridge (UK). Powdered gypsum samples (~5 mg) were dissolved in deionized water at 45 °C overnight. The effluent containing the aqueous sulfate from the dissolution was then separated, and a barium chloride solution (50 g/L) was added to induce $BaSO_4$ precipitation. The $BaSO_4$ was rinsed with 6 M HCl to remove carbonates, and subsequently rinsed 3 times with deionized water. The samples were then dried at 45 °C overnight.

For $\delta^{18}O_{SO4}$, a High Temperature Conversion Element Analyzer (TC/EA) was used to pyrolyze the $BaSO_4$ at 1450 °C and produce CO, which was measured by continuous flow Gas Source Isotope Ratio Mass Spectrometry (ThermoScientific Delta V Plus). All $\delta^{18}O_{SO4}$ are reported relative to V-SMOW (Vienna-Standard Mean Ocean Water). Samples were run in triplicate, alongside the NBS-127 Standard (8.6‰), and the standard deviation of the replicate analyses was better than 0.5‰ (1σ).

For $\delta^{34}S_{SO4}$, the $BaSO_4$ was combusted at 1030°C in a Flash Elemental Analyzer (Flash-EA), and the sulfur dioxide produced was measured by continuous flow Gas Source Isotope Ratio Mass Spectrometry (ThermoScientific, Delta V Plus).

All $\delta^{34}S_{SO4}$ are reported relative to VCDT (Vienna-Canyon Diablo Troilite). Samples for sulfur isotope analysis were run in duplicate, alongside the NBS-127 standard (20.3‰). The reproducibility (1σ) of $\delta^{34}S_{SO4}$ of the duplicate analyses was better than 0.2‰, similar to the long-term reproducibility of the NBS-127 over the run (0.2‰).

3.3.2. $\delta^{18}O$ and δD of gypsum hydration water (GHW)

The GHW of 8 samples was extracted by slowly heating each sample (~200 mg) to 400 °C, *in vacuo,* using a bespoke offline extraction system consisting of six vacuum lines contained within a modified gas chromatography (GC) oven, following the method of Gázquez et al. (2015a). Oxygen ($\delta^{18}O$) and hydrogen (δD) isotopes in GHW were measured simultaneously by cavity ring down spectroscopy (CRDS) in the Godwin Laboratory at the University of Cambridge (UK) using a L1102-i Picarro water isotope analyzer (Hodell et al., 2012; Evans et al., 2015; Chen et al., 2016). All results are reported in parts per thousand (‰) relative to V-SMOW. Calibration of results to V-SMOW was achieved by analyzing internal standards before and after each set of 10 or 12 samples. Internal standards were previously calibrated against V-SMOW, GISP, and SLAP. External error (1σ) of the method was ±0.1‰ for $\delta^{18}O$ and ±0.6‰ for δD, as estimated by repeated analysis (n=3) of an analytical grade standard, extracted together with the samples in each run of the extraction apparatus (Gázquez et al., 2015a).

3.3.3. Strontium isotopes

Strontium isotope ($^{87}Sr/^{86}Sr$) measurements were made by thermal ionization mass spectrometry (Thermo-Scientific Triton Plus MC-TIMS) at the University of Cambridge. Approximately 2.5 mg of powdered gypsum (n=3) was processed for isotopic analysis. Gypsum was ground to a fine powder and dissolved in deionized water. Carbonate samples were also ground placed in deionized water for 24 h to extract soluble salts. The supernatant fluid was stored for isotopic analysis (n=2). The carbonate samples themselves (n=2) were prepared for isotope analysis by treating the samples with methanol, 10% ammonium hydroxide and water washes (to mechanically remove clays and adsorbed ions), each step performed in triplicate. To isolate the carbonate phase, the solid sample was dried, weighed and placed in a volume of 0.1M HCl containing 110% of the acid required for complete dissolution of the carbonate, calculated to avoid elemental variation generated by incomplete dissolution.

An aliquot of each sample solution containing approximately 300 ng of strontium was dried down, dissolved in 200 µl 3M HNO_3 and refluxed at 80 °C for 3 hours. Strontium was separated using Eichrom Sr Spec resin with 100 µm to 150 µm mesh particle size in clean lab conditions. The separated Sr was dried down, refluxed in 3N HNO_3 and subsequently dried down once again. Samples were then loaded onto degassed single Re filaments together with 1 µl of tantalum phosphate activator. A current of ~0.8A was continuously applied during the loading. The evaporation filament is heated manually until a stable signal between 4V and 6 V of ^{88}Sr on a $10^{11}\Omega$ resistor was reached. Data acquisition was comprised of 10 blocks of 20 measurements with a ~8 s integration time in static mode. Results were normalized to $^{88}Sr/^{86}Sr$ 0.1194 with an exponential

fractionation correction. Runs were bracketed with the NBS 987 standard. Eleven analyses of NBS 987 during 2 months before and after this study gave a mean value of 0.710253 (2σ = 0.000007). Blanks were <250 pg and negligible for the Sr concentration of these samples.

3.4. Microthermometry of fluid inclusions

The method for microthermometric analysis of fluid inclusions in gypsum closely followed that described by Attia et al. (1995) and Evans et al. (2015). Thin (<1mm) sections of gypsum were obtained by cleaving the mineral along 010 planes using a razor blade. The fragments were placed in a Linkam THMSG600 heating-freezing stage attached to a Zeiss Axio Scope.A1 microscope. The ice melt temperature (T_m) of primary fluid inclusions (identified as described in Attia et al. 1995) in samples CT-15B (n=11), CT-21B (n=10) and CT-23 (n=4) was determined following the procedure described by Evans et al. (2015). T_m was recorded to within 0.1 °C and reproduced at least twice for each inclusion with an error of ±0.2 °C. Salinities of the fluid inclusions were calculated from the final T_m and expressed as weight % NaCl equivalent (Bodnar, 1993).

4. Results

4.1. Mineralogy

The cave host-rock comprises an alternate sequence of limestone (grey materials) and dolostone (reddish materials) beds that outcrop inside and outside the cave (Fig. 2 A and B). Most of the concretions, infillings and coatings in the Passage of the Debris and the Hall of the Chandeliers are made of microcrystalline gypsum (Fig. 3C) and halite (NaCl) (Fig. 3G), with minor dolomite

and celestine ($SrSO_4$) and occasionally brownish sugary-textured calcite (Fig. 3D). The mineralogical analyses confirm that the microcrystalline coatings in the ceiling of the Hall of the Chandeliers and in the selenite crystals of the 'chandeliers' (Fig. 3E) are made of high-purity gypsum. The apices of some of the chandeliers are made of a halite cylinder, containing traces of celestine (Fig. 3F). The 'boxwork' structures of the 'Hall of the Boxwork' is composed of dolomite blades (with minor calcite), covered by gypsum coatings (Fig. 3G). In the Hall of the Eccentrics, the 'blister' speleothems are made of gypsum, while the inner stalactites are composed of aragonite (Fig. 3I). All the analyzed stalactites in this chamber are composed of aragonite, which in places display single gypsum crystals hanging from their tips (Fig. 3J).

4.2. Stable isotopes

4.2.1 Sulfur and oxygen in sulfate

The $\delta^{34}S$ values in gypsum speleothems range from 16.7‰ to 20.7‰, and the $\delta^{18}O_{SO4}$ in sulfate ranges from 3.0‰ to 11.6‰. The $\delta^{34}S$ and $\delta^{18}O_{SO4}$ show a positive correlation with slope of 1.3 (Fig. 4). The gypsum coatings from the Passage of the Boxwork display higher $\delta^{34}S$ and $\delta^{18}O_{SO4}$, within the range of modern marine sulfate (~20‰ and ~9‰, respectively). The rest of samples fall out of this range and generally have lower $\delta^{34}S$ and $\delta^{18}O_{SO4}$ values.

4.2.2 $\delta^{18}O$ and δD of gypsum hydration water

The $\delta^{18}O$ and δD in GHW of speleothems from El Orón-Arco Cave range from 2.0‰ to 5.8‰ and from -24.8‰ to -13.6‰, respectively. The oxygen and hydrogen isotope composition of the parent water from which the gypsum formed

is calculated by using the values of GHW and known fractionation factors ($\alpha^{18}O_{gypsum\text{-}water}$ and $\alpha D_{gypsum\text{-}water}$), which are practically insensitive to temperature between 5 °C and 30 °C (Gázquez et al., 2017a; Liu et al., 2018). The $\alpha D_{gypsum\text{-}water}$ is relatively sensitive to water salinity ($3x10^{-5}$ per g/L of NaCl between 30 g/L and 300 g/L), whereas $\alpha^{18}O_{gypsum\text{-}water}$ is not affected by salinities less than 150 g/L of NaCl (Gázquez et al., 2017a). Gypsum samples in this study precipitated mostly from solutions with salinities around 130-150 g/L (see section 4.3). We use fractionation factors at 150 g/L ($\alpha^{18}O_{gypsum\text{-}water}$ of 1.0033 and $\alpha D_{gypsum\text{-}water}$ of 0.985; Gázquez et al, 2017a). Changes in temperature of ±5°C, result in uncertainty of ±0.5‰ in the calculated values of δD of the mother water, which is insignificant given the analytical precision of the measurements (±0.6‰). Changes in salinity of ±50 g/L would result in uncertainties of ±1.5‰ in δD of the mother water, which is also irrelevant for our application.

By applying the selected isotope fractionation factors to the isotope composition of GHW, we found that the $\delta^{18}O$ of the speleothem-forming water ranges from -0.7‰ to 2.5‰, while δD ranges from -9.9‰ to 3.2‰. The speleothems from the Hall of the Eccentrics show the lower $\delta^{18}O$ and δD values, whereas gypsum in the Hall of the Chandeliers precipitated from a solution more enriched in the heavy isotopes (Table 1 and Fig. 5). Together, the $\delta^{18}O$ and δD of the speleothem-forming water values describe a line with a slope of ~3.3.

4.2.3. Strontium isotopes

The $^{87}Sr/^{86}Sr$ of the analyzed gypsum speleothems is 0.70815±0.00005 (n=3). The lowest value corresponds to the gypsum ‘blisters’ from the Hall of the

Eccentrics (0.708095), while the highest $^{87}Sr/^{86}Sr$ value is found in the gypsum coatings from the Passage of the Debris (0.708188). The carbonate host-rock shows consistently lower $^{87}Sr/^{86}Sr$ values of 0.70779±0.00007 (n=2). The $^{87}Sr/^{86}Sr$ of the water-soluble salt leaches from the host-rock display intermediate $^{87}Sr/^{86}Sr$ values between the gypsum speleothems and the host-rock of 0.70796±0.00004 (n=2) (Fig. 6).

4.3. Fluid inclusions

The ice melt temperatures (T_m) of primary fluid inclusions in gypsum speleothems range from -15.7 ^oC to -3.3 ^oC (n=27), corresponding to salinities from 19.2 to 5.4 wt. % eq. NaCl. The gypsum 'chandeliers' (Fig. 3E) have the lowest T_m (-10.7±2.5^oC; n=12) and therefore, the highest salinity of fluid inclusions (14.2±2.5 wt. % eq. NaCl), while the gypsum spar on the tip of an aragonite stalactite (CT-23A1) from the Hall of the Eccentrics displays the highest T_m (-5.5±1.9^oC; n=4) and lowest salinities (8.2±2.5 wt. % eq. NaCl). Another gypsum spar (CT-21A; Fig. 3J) from the same chamber shows intermediate T_m values (-9.9±2.4^oC; n=11) and salinities (13.7±2.4 wt. % eq. NaCl). Altogether, the mean T_m is -9.5±2.9^oC and the salinity is 13.2±3.2 wt. % eq. NaCl, on average (Fig. 7).

5. Discussion

5.1. Geomorphological and mineralogical evidence for sea salt weathering

There is no physical evidence of either phreatic or vadose dissolution that would support conventional karstification mechanisms operating in the El Orón-Arco Cave today. As in many other ‘flank margin coastal caves’, El Orón-Arco Cave lacks both the typical morphologies related to water flow and indicators of subaqueous carbonate dissolution (e.g. scallops, smoothed surfaces or cupolas, etc.) (Mylroie and Mylroie, 2007). In contrast, the cavity displays clear evidence of recent mechanical weathering processes (Fig. 8). It should be noted that, while there is no evidence for conventional speleogenesis within El Orón-Arco Cave, it cannot be ruled out that the initial stages of the cave speleogenesis were controlled by phreatic or vadose dissolution processes. This may have led to the enlargement of the subterranean network before the stage of physical weathering. The signs of such hypothetical dissolution mechanisms might have been masked by the subsequent effects of subaerial sea salt weathering. In addition, the motion of faults system that runs parallel to the cliff of the Cabo Tiñoso may have played a main role in the initial stages of the cave formation by creating preferential groundwater pathways that favored the karstification of the carbonate host-rock.

The unsorted carbonate host-rock fragments (<1 mm to tens of centimeters) that rest against the walls of the ‘Passage of the Debris’ and in the entrance of the ‘Passage of the Boxwork’ provide strong evidence of a mechanical cave-forming mechanism that has operated in the cave at least in recent times (Fig. 2D). The cave walls and ceilings are made of easily detachable rock that crack and

eventually fall naturally to the cave floor, accumulating as piles of unsorted rubble. This process is currently active and was observed during our visits to the cave. Indeed, the accumulation of rock debris in the smaller passages (e.g. the access to the Passage of the Boxwork) represents a serious challenge when accessing the cave, since these galleries are prone to obstruction and frequently need to be unblocked by speleologists.

Mineralogical analyses of cave wall materials reveal the presence of minerals typically derived from evaporated seawater, including halite, gypsum and occasionally calcite (Table 1). The cave host-rock is predominantly composed of greyish limestone and reddish dolostone, the latter containing small amounts of iron oxides. In the planes of the carbonate beds, whitish and yellowish saline concretions and efflorescences are observed projecting out into the cave (Figs. 2C and 3C). A mechanism is needed to explain the presence of evaporitic minerals within the host-hock material and the formation of weathered debris on the cave floor.

We suggest that capillary action and infiltration of seawater through the carbonate formation of Cabo Tiñoso followed by evaporation of the solution in the cave results in the crystallization of evaporites in planes and pores, leading to ‘gypsum/halite wedging’ of the host-rock (Fig. 8). In the cave environment, evaporation of infiltrated seawater is favored by the relatively high air temperature in the cave (~19 °C during our visit in January 2012) and likely low relative humidity. Although relative humidity has not been measured in the cave, the presence of halite strongly indicates relatively dry conditions because halite

394 dissolves if atmospheric relative humidity is above ~73% (Wexler and Hasegawa,
395 1954; Oerter et al., 2018).
396
397 The crystallization pressure generated by the formation of salts in pore spaces
398 (e.g. Goudier and Viles, 1997; Rodriguez-Navarro and Doehne, 1999) caused
399 fracking and disaggregation of the original Triassic dolostones and limestones.
400 Moreover, the motion of the faults in the Cabo Tiñoso formation and eustatic sea-
401 level changes may have played a role in the ejection of the disaggregated
402 materials (Fig. 8). During periods of relatively high sea-level, parts of the cave
403 passage (today mostly between 0 and 50 m a.s.l.) were likely submerged in a
404 brackish aquifer. In this scenario, calcium ions could be released to the solution
405 from the limestones and dolostones and, in combination with the SO_4^{2-} from
406 seawater, result in the oversaturation of the solution for gypsum ($SI_{gyp}>0$) and
407 subsequent mineral precipitation in cracks and pores of the carbonate host-rock
408 (see section 5.3) (Fig. 8A). During periods of relatively low sea-level, these
409 primary evaporites would dissolve because of circulation of meteoric/brackish
410 water mixture undersaturated in gypsum and halite (Fig. 8B). The solution
411 enriched in dissolved salts could evaporate in the voids of the rock and the
412 crystallization pressure generated by the secondary minerals would result in a
413 significant sea salt weathering mechanism, as shown in Fig. 8.
414
415 The ‘gypsum/halite wedging’ process described above is a relatively uncommon
416 mechanism in caves and has only been described in a few subterranean sites,
417 including the Mammoth cave system in Kentucky, USA (White and White, 2003),
418 the Friars Hole cave system in West Virginia, USA (Jameson, 1991), and some

caves of the Nullarbor Plain, Australia (Lowry and Jennings 1974). Also, it is well documented that similar processes of capillary action of saline waters and crystallization of salts are responsible for the decay of building materials and limestone sculptures (e.g. Cardell et al., 2008; Gómez-Laserna et al. 2013; Gázquez et al., 2015b) and contribute to the formation of geomorphological features, such as honeycombs, alveoles and tafoni, especially in dry regions (Prebble, 1967; Beaumont, 1968; Bradley et al., 1978; Goudie and Day, 1980; Mustoe, 1982; Mottershead, 1989). We use stable isotopes to test the sea salt weathering hypothesis in sections 5.2 and 5.3.

5.2. Identification of sulfate sources

The $\delta^{18}O_{SO4}$ and $\delta^{34}S$ of secondary gypsum deposits in El Orón-Arco Cave are generally lower than those expected for gypsum formed solely from modern seawater ($\delta^{18}O_{SO4}$ ~9‰ and $\delta^{34}S$ ~21‰) (Fig. 4). The only samples that show seawater-like sulfate isotopic composition are the gypsum crusts on the dolomite boxwork formations found in the Passage of the Boxwork. In a $\delta^{18}O_{SO4}$-$\delta^{34}S$ plot, the gypsum samples are positively correlated (slope of 1.3) and have $\delta^{18}O_{SO4}$ and $\delta^{34}S$ down to 3‰ and 16.5‰, respectively.

During crystallization from the solution, gypsum precipitates with a negligible sulfur isotope fractionation (Raab and Spiro, 1991; Van Driessche et al., 2016), but as much as a 3‰ offset for oxygen isotopes, although the latter isotopic fractionation factor is poorly constrained (Van Driessche et al., 2016). If the sulfate that formed the gypsum was derived directly from seawater, the $\delta^{18}O_{SO4}$ and $\delta^{34}S$ of the gypsum should reflect seawater values. Subsequent solution-

444 reprecipitation of the gypsum in water with a similar $\delta^{18}O_{SO4}$ and $\delta^{34}S$ should not
445 alter the $\delta^{18}O_{SO4}$ and $\delta^{34}S$ of the gypsum significantly (Evans et al., 2015). Our
446 observations in El Orón-Arco Cave show that gypsum speleothems have
447 significantly lower oxygen and sulfur isotope values than modern marine sulfate,
448 so direct gypsum precipitation from seawater cannot completely explain our
449 observations.
450
451 The lower $\delta^{18}O_{SO4}$ and $\delta^{34}S$ may be derived from either (i) oxidation of isotopically
452 ^{34}S-depleted sulfur in sulfide minerals (e.g. pyrite) hosted in the carbonate
453 bedrock (e.g. Audra et al., 2015) or (ii) the oxidation of aqueous sulfide previously
454 reduced from marine sulfate by bacteria. Both sulfide minerals and aqueous
455 sulfide take at least one of their oxygen atoms from water upon oxidation,
456 producing sulfate that is more depleted in both the ^{34}S and ^{18}O isotopes.

457 No sulfide mineralization has been identified in the cave or in our samples by
458 mineralogical analyses. However, this region, including the nearby Sierras of
459 Cartagena and Mazarrón (~20 km from El Orón-Arco Cave), hosts important Zn-
460 Pb-Cu-Ag-Fe sulfide deposits that are related to volcanism and epigene
461 hydrothermal activity (Esteban-Arispe et al., 2016). Most regional sulfide minerals
462 have $\delta^{34}S$ values ranging from +2‰ to +15‰, and thus represent a potential
463 source of ^{34}S-depleted sulfates to the cave system compared to marine sulfate
464 (Table 1). We suggest that migration of fluids from depth through the faults
465 system of Cabo Tiñoso can explain the $\delta^{18}O_{SO4}$ and $\delta^{34}S$ values. This mechanism
466 assumes oxidation of ^{34}S-depleted sulfide to sulfate occurred in deeper strata,
467 followed by mobilization to the cave level and mixing with marine sulfate. Indeed,
468 in other caves affected by ‘gypsum wedging’ (e.g. Mammoth cave system,

469 Kentucky, US), the $\delta^{34}S$ values in gypsum (-12‰ to +12‰) have been interpreted
470 as being completely derived from oxidation of pyrite (Metzger et al., 2015). Thus,
471 we suggest that, although oxidation of sulfide minerals is not the primary source
472 of sulfate for gypsum precipitation in the El Orón-Arco Cave, mixing with marine
473 sulfate can explain the observed $\delta^{34}S$ values. As for $\delta^{18}O_{SO4}$, the relatively low
474 $\delta^{18}O_{SO4}$ observed in El Orón-Arco Cave can also be explained by oxidation of
475 sulfide, which incorporates oxygen atoms from meteoric water that is typically
476 depleted in the ^{18}O isotope (Van Stempvoort and Krouse, 1994; Onac et al.,
477 2011).

478 Alternatively, mixing of aqueous sulfate derived from the oxidation of sulfide
479 (previously reduced from seawater sulfate by bacteria) and marine sulfates may
480 explain the relatively low $\delta^{34}S$ and $\delta^{18}O_{SO4}$ in the gypsum speleothems in this
481 cave. Microbial sulfate reduction produces ^{34}S-depleted sulfides, with maximum
482 observed depletions of -72‰ (Sim et al., 2011), whereas the oxidation of sulfide
483 to elemental sulfur has a far lower sulfur isotope fractionation, producing
484 enrichments in the ^{34}S isotope on the order of +8‰ (Zerkle et al., 2016). Complete
485 oxidation of elemental sulfur to sulfate does not produce significant sulfur isotope
486 fractionation (Zerkle et al., 2016 and references therein). Bacterial sulfur
487 reduction and re-oxidation results in sulfates with low $\delta^{34}S$ and $\delta^{18}O_{SO4}$ values.
488 However, this mechanism requires anoxic conditions that may have never
489 occurred in El Orón-Arco Cave, where the presence of organic matter is scarce,
490 and oxygen concentration may have not been a limiting factor. In summary, the
491 $\delta^{18}O_{SO4}$ and $\delta^{34}S$ observed in El Orón-Arco Cave can be explained by mixing of

492 seawater sulfate and isotopically lower sulfate derived from oxidation of sulfide
493 minerals in depth and transported to the cave level though the faults system.

494

495 **5.3. Modes of gypsum/halite precipitation**

496 Gypsum precipitation has been identified as the cause of aqueous sulfate
497 depletion in the fronts of marine water intrusions in coastal aquifers (Gomis-
498 Yagües et, 2000; Boluda-Botella et al., 2004). The meteoric-seawater mixture in
499 the mixing zone of coastal aquifers is generally undersaturated in gypsum
500 (SI_{gyp}<0). However, the intrusion front contains relatively high concentrations of
501 dissolved ions (mostly SO_4^{2-}, Cl^-, Ca^{2+}, Mg^{2+} and Na^+) that can interact with the
502 carbonate bedrock. Magnesium and sodium can displace calcium in limestones
503 and dolostones, resulting in an increase of calcium in the solution that, together
504 with high sulfate concentrations in seawater, can lead to SI_{gyp}>0 and gypsum
505 precipitation (Gomis-Yagües et, 2000; Boluda-Botella et al., 2004).

506

507 Strontium isotope ratios provide a tracer between marine-sourced fluids and other
508 strontium-bearing fluids as each endmember is often characterized by different
509 strontium concentrations and $^{87}Sr/^{86}Sr$. Because of the long residence time of
510 strontium relative to the mixing time of the ocean, $^{87}Sr/^{86}Sr$ is homogeneous in
511 the global ocean. Strontium in modern seawater has a radiogenic $^{87}Sr/^{86}Sr$
512 (0.70916) which differs significantly from other sources of strontium such as fluids
513 produced from the weathering of silicate (>0.720) and carbonate (<0.708)
514 lithologies (Elderfield, 1986). The host-rock of El Orón-Arco Cave shows relatively
515 low $^{87}Sr/^{86}Sr$ values (0.70779±0.00007), that are similar to those expected for
516 Triassic marine carbonates (0.7078; McArthur et al., 2001). The $^{87}Sr/^{86}Sr$ of the

gypsum speleothems is 0.70815±0.00005 (n=3), thus displaying higher $^{87}Sr/^{86}Sr$ than those of the host-rock, but considerably lower $^{87}Sr/^{86}Sr$ than modern seawater. The soluble-salts leaches from the host-rock have intermediate $^{87}Sr/^{86}Sr$ between the Triassic carbonate and the speleothems (Fig. 6). This suggests that strontium in the speleothem-forming solution comes primarily from the Triassic carbonate (~75%) dissolution by brackish aquifer water before gypsum precipitation, rather than from modern marine strontium (~25%). This mechanism of host-rock dissolution was therefore also responsible for enhanced calcium concentration in the solution that lead to $SI_{gyp}>0$ and gypsum precipitation in cracks of the host-rock.

The gypsum precipitation process often requires evaporation of the fluid for the solution to reach $SI_{gyp}>0$, as observed in other caves (Forti, 1996; Filippi et al., 2011; Gázquez et al., 2005c; 2017b). In such situations, $\delta^{18}O$ and δD of the evaporated water normally produce a line in $\delta^{18}O$ vs δD space with a slope less than 8. However, by adding calcium and sulfate to the solution, gypsum can precipitate directly from the solution with little evaporative enrichment. We test both hypotheses by studying the stable isotopes of GHW. Because the $\delta^{18}O$ and δD is recorded by the structurally-bound hydration water of evaporative gypsum, evaporative processes (or lack therefor) can be constrained (Evans et al., 2015, 2018; Gázquez et al., 2017b; 2018).

The $\delta^{18}O$ and δD values of the speleothem-forming solution in El Orón-Arco Cave do not fall in the field of non-evaporated seawater ($\delta^{18}O$ and δD ~ 0‰), nor do they indicate gypsum precipitation from evaporated seawater to the point of

gypsum saturation (e.g. Evans et al., 2015; Gázquez et al., 2017a), which displays much greater $\delta^{18}O$ and δD values than observed. Instead, the isotope values of the speleothem-forming water fall on an evaporation line that probably departed from an intermediate point between seawater values and the meteoric water seepage ($\delta^{18}O$ of ~-5‰ and δD of ~-40‰ in SE Iberian Peninsula; e.g. Gázquez et al., 2017b) (Fig. 5). This demonstrates that (1) the speleothem-forming solution was a mixture of fresh-meteoric water and seawater and (2) that this solution underwent significant evaporation in the cave before gypsum precipitation.

Surprisingly, the salinity of the speleothem-forming waters (13.2±3.2 wt. % eq. NaCl) was considerably higher than expected for gypsum formed from an evaporated brackish solution (i.e. ~4-8 wt. % eq. NaCl; Attia et al., 1995; Natalicchio et al., 2014; Evans et al., 2015) and more similar to the salinity of fluid inclusions in purely evaporated seawater to gypsum saturation (i.e. ~12-14 wt. % eq. NaCl). This apparent discrepancy between the results of stable isotopes in GHW and salinity of fluid inclusions can be explained by a mechanism involving (1) remobilization of halite/gypsum previously precipitated in cracks of the host-rock that is easily dissolved by water undersaturated in halite and gypsum (e.g. meteoric/seawater mixture); and (2) evaporation once the solution reaches the cave, resulting in precipitation of gypsum with relatively high salinity of fluid inclusions, but relatively low $\delta^{18}O$ and δD values (Fig. 8). Alternatively, partial post-depositional isotopic exchange of GHW with an isotopically ^{18}O-depleted source (i.e. meteoric waters) or gypsum reprecipitation, particularly in the case of microcrystalline gypsum speleothems (e.g. Fig. 3I), could be argued (Sofer, 1978;

567 Pierre, 2018). However, this alteration may also derive secondary fluid inclusions
568 with lower salinities, which have not been observed in the analyzed samples from
569 El Orón-Arco Cave.
570
571 **6. Conclusions**
572 We demonstrate that the genesis of El Orón-Arco Cave was linked to the motion
573 of faults that runs parallel to the cliff of the Cabo Tiñoso, and to salt weathering
574 of the carbonate host-rock by infiltration and capillary action of seawater that
575 subsequently evaporates within the cave, leading to precipitation of evaporite
576 minerals (gypsum and halite) in pores and planes of the carbonate. The
577 crystallization pressure of salts produces cracking of the host-rock at different
578 scales. The detached rock fragments accumulate in piles that rest against the
579 cave walls. The same process of seawater infiltration is responsible for the
580 precipitation of gypsum and halite in speleothems of uncommon morphology,
581 including gypsum chandeliers, halite soda-straws and gypsum blisters.
582
583 The source of sulfates for gypsum precipitation is predominantly marine, although
584 the $\delta^{34}S$ and $\delta^{18}O_{SO4}$ results are lower than those expected during the formation
585 from modern seawater alone, suggesting a mixing of marine source fluids with an
586 isotopically depleted sulfate source (i.e. oxidation of sulfide minerals). The
587 isotopic composition of GHW and relatively high salinity of fluid inclusion in
588 gypsum crystals can be explained by recycling of evaporites (gypsum and halite)
589 from previous stages and gypsum reprecipitation in the form of speleothems. The
590 salt-weathering mechanism proposed here for the formation of El Orón-Arco
591 Cave is probably not an isolated case and may be responsible for the formation

of other caves elsewhere, both in coastal environments of dry regions and saline settings (e.g. caves associated to saline diapirs).

Acknowledgements

The authors are grateful to all the speleologists that collaborated in the survey in El Orón-Arco Cave, and to Dr. Gilad Antler and Mr. James Rolfe for assistance with $\delta^{34}S$ and $\delta^{18}O$ analyses in sulfates. This research was funded by the ERC WIHM Project (#339694) to DAH, the Water Resources and Environmental Geology Research Group (University of Almería) and the Department of Physics of Condensed Matter at University of Valladolid (Spain). FG was financially supported by the "HIPATIA" research program of the University of Almería. Surveys and sampling in the cave were supported by the Federación de Espeleología de la Región de Murcia and RODCLE®.

7. References

Attia, O. E., Lowenstein, T.K., Wali, A.M.A. 1995. Middle Miocene gypsum, Gulf of Suez: marine or nonmarine? J. Sediment. Res. 65A (4), 614–626.

Audra, Ph., Palmer A. 2015. Research frontiers in speleogenesis. Dominant processes, hydrogeological conditions and resulting cave patterns. Acta Carsolog. 44(3), 315-348.

Audra, Ph., Gázquez, F., Rull, F., Bigot, J.Y., Camus, H. 2015. Hypogene Sulfuric Acid Speleogenesis and rare sulfate minerals in Baume Galinière Cave (Alpes-de-Haute-Provence, France). Record of uplift, correlative cover retreat and valley dissection. Geomorphology 247, 25-34.

Beaumont, P. 1968. Salt weathering on the margin of the Great Kavir, Iran. Geol. Soc. Am. Bull. 79, 1683-1684.

Bodnar, R. 1993. Revised equation and table for determining the freezing point de-pression of H2O–NaCl solutions. Geochim. Cosmochim. Acta 57 (3), 683–684.

Boluda-Botella, N., Gomis-Yagües, V., Ruiz-Beviá, F., Saquete-Ferrándiz, MD. 2004. Gypsum precipitation/dissolution during seawater intrusion. 18th Salt Water Intrusion Meeting. Cartagena (Spain).

Bradley, W.C., Hutton, J.T., Twidale, C.R. 1978. Role of salts in development of granitic tafoni, South Australia, J. Geol. 86, 647-654.

Cardell, C., Benavente, D., Rodriguez-Gordillo, J. 2008. Weathering of limestone building material by mixed sulfate solutions. Characterization of stone microstructure, reaction products and decay forms. Mate Charact, 59, 1371-1385.

Chen, F., Turchyn A.V., Kampman N., Hodell D., Gazquez, F., Maskell, A. Bickle, M.J. 2016. Isotopic analysis of sulfur cycling and gypsum vein formation in a natural CO_2 reservoir. Chem. Geol. 436, 72-83.

Davis, D.G. 2000. Extraordinary features of Lechuguilla Cave, Guadalupe Mountains. J. Cave Karst Stud. 62, 147-157.

Elderfield, H. 1986. Strontium isotope stratigraphy. Palaeogeogr. Palaeoclimatol, Palaeoecolog. 57 (1), 71–90.

Esteban-Arispe, I., Velasco-Roldán, F., Boyce, A.J, Morales-Ruano, S., Yusta, I., Carrillo-Rosúa, J. 2016. Unconventional non-magmatic sulfur source for the Mazarrón Zn-Pb-Cu-Ag-Fe epithermal deposit (SE Spain). Ore Geol. Rev., 72, 1102-1115.

641 Evans, N. P., Turchyn, A. V., Gázquez, F., Bontognali, T. R. R., Chapman, H. J.
642 and Hodell D. A. 2015. Coupled measurements of $\delta^{18}O$ and δD of hydration
643 water and salinity of fluid inclusions in gypsum from the Messinian Yesares
644 Member, Sorbas Basin (SE Spain). Earth Planet. Sci. Lett. 430, 499–510.
645 Evans, N.P., Bauska, T.K., Gázquez, F., Brenner, M., Curtis, J. H., Hodell, D. A.
646 2018. Quantification of drought during the collapse of the classic Maya
647 civilization. Science, 361 (6401), 498–501.
648 Filippi, M., Bruthans J., Palatinus L., Zare M. and Asadi N. 2011. Secondary halite
649 deposits in the Iranian salt karst: general description and origin. Int. J. Speleol,
650 40 (2), 141-162.
651 Forti, P. 1996. Speleothems and cave minerals in gypsum caves. Int. J. Speleol.
652 25, 91–104.
653 García-Tortosa, F.J., López-Garrido, A., Sanz de Galdeano, C. 2000. Las
654 unidades de Cabo Tiñoso y Peñas Blancas: Revisión y caracterización
655 estratigráfica de las unidades alpujárrides del sector entre Mazarrón y
656 Cartagena (Murcia, España). Estud. Geol.-Madrid, 56, 31-40.
657 Gázquez, F., Mather, I., Rolfe, J., Evans, N.P., Herwartz D., Staubwasser M.,
658 Hodell D.A. 2015a. Simultaneous analysis of $^{17}O/^{16}O$, $^{18}O/^{16}O$ and $^{2}H/^{1}H$ of
659 gypsum hydration water by cavity ring-down laser spectroscopy. Rapid
660 Commun. Mass Spectrom. 29, 1997–2006.
661 Gázquez, F., Calaforra, J. M., Forti, P., DeWaele, J., Sanna, L. 2015b. The role
662 of condensation in the evolution of dissolutional forms in gypsum caves: study
663 case in the karst of Sorbas (SE Spain). Geomorphology 229, 100–111.

664 Gázquez, F., Rull, F., Medina, J., Sanz-Arranz, A., Sanz, C. 2015c. Linking
665 groundwater pollution to the decay of 15th-century sculptures in Burgos
666 Cathedral (northern Spain). Environ. Sci. Pollut. Res. 22, 15677–15689.
667 Gázquez F., Evans N.P. and Hodell D.A. 2017a. Precise and accurate isotope
668 fractionation factors ($\alpha^{17}O$, $\alpha^{18}O$ and αD) for water and $CaSO_4 \cdot 2H_2O$ (gypsum).
669 Geochim. Cosmochim. Acta 198, 259–270.
670 Gázquez F., Calaforra J.M., Evans N.P. and Hodell D.A. 2017b. Using stable
671 isotopes ($\delta^{17}O$, $\delta^{18}O$ and δD) of gypsum hydration water to ascertain the role
672 of water condensation in the formation of subaerial gypsum speleothems.
673 Chem. Geol. 452, 34–46.
674 Gázquez F., Morellón M., Bauska T., Herwartz D., Surma J., Moreno A.,
675 Staubwasser M., Valero-Garcés B., Delgado-Huertas A., Hodell D.A. 2018.
676 Triple oxygen and hydrogen isotopes of gypsum hydration water for
677 quantitative paleo-humidity reconstruction. Earth Planet. Sci. Lett. 481, 177–
678 188.
679 Ginés A., Ginés. J. 2007. Eogenetic karst, glacioeustatic cave pools and
680 anchialine environments on Mallorca Island: a discussion of coastal
681 speleogenesis. Int. J. Speleol, 36, 57-67.
682 Gómez-Laserna, O, Olazabal, M.A, Morillas, H, Prieto-Taboada, N, Martinez-
683 Arkarazo, I, Arana, G, Madariaga, J.M. 2013. In-situ spectroscopic
684 assessment of the conservation state of building materials from a Palace
685 house affected by infiltration water. J Raman Spectrosc. 44, 1277–1284.
686 Gomis-Yagües, V., Boluda-Botella, N. Ruiz-Bevia, F. 2000. Gypsum precipitation
687 as an explanation for the decrease of sulfate concentration during seawater
688 intrusion. J. Hydrol. 228, 48-55.

689 Gordillo, A., Espinosa, J., Martin, J.M., Pérez, A. 1972. Mapa Geológico
690 Cartagena. 1:50.000. IGME.
691 Goudie, A.S., Viles, H. A. 1997. Salt weathering. Chichester: Wiley, 241 pp.
692 Goudie, A.S., Day, M. J. 1980. Disintegration of fan sediments in Death Valley,
693 California, by salt weathering. Phys. Geogr. 1, 126-137.
694 Hodell, D.A., Turchyn, A.V., Wiseman, C.J., Escobar, J., Curtis, J.H., Brenner,
695 M., Gilli, A., Mueller, A.D., Anselmetti, F., Ariztegui, D., Brown, E.T. 2012. Late
696 glacial temperature and precipitation changes in the lowland Neotropics by
697 tandem measurement of $\delta^{18}O$ in biogenic carbonate and gypsum hydration
698 water. Geochim. Cosmochim. Acta 77, 352–368.
699 Jameson, R.A. 1991. Concept and classification of cave breakdown: An analysis
700 of patterns of collapse in Friars Hole Cave System, West Virginia, in Kastning,
701 E.H., Kastning, K.M. (eds.), Appalachian karst. National Speleological Society,
702 Huntsville, AL, p. 35-44.
703 Liu, T., Artacho, E., Gázquez, F., Walters, G., Hodell, D.A. 2018. Prediction of
704 Equilibrium Isotopic Fractionation of the Gypsum/Bassanite/Water System
705 using First-Principles Calculations, Geochim. Cosmochim. Acta. 244, 1-11.
706 Llamusí, J.L., Ingles, S., Ros, A., Rodríguez, A., Pérez, C. 1990. Cavidades
707 Submarinas del Cabo Tiñoso (Cartagena). Revista Caliza, 1, 24.
708 Lowry, D.C. Jennings, J.N. 1974. The Nullarbor karst Australia: Zeitschrift für
709 Geomorphologie. 18, 35-81.
710 Maltsev, V.A., Self, C.A. 1992. Cupp-Coutunn cave system, Turkmenia, Central
711 Asia. Proceedings of the University of Bristol Speleological Society 19: 117-
712 149.

713 Martín, D. 2004. Programa para el análisis por difracción de rayos X. Método en
714 Polvo (XPowder). Universidad de Granada.
715 McArthur, J., Howarth, R., Bailey, T. 2001. Strontium isotope stratigraphy:
716 LOWESS version 3: best fit to the marine Sr-isotope curve for 0–509 Ma and
717 accompanying look-up table for deriving numerical age. J. Geol.109 (2), 155–
718 170.
719 Metzger, J.G., David A. Fike, D.A., Osburn, G.R., Guo, C.J., Aadison, A.N. 2015.
720 The source of gypsum in Mammoth Cave, Kentucky. Geology. 43, 187–190.
721 Moore, D.G. 1954. Origin and development of sea caves. Nat. Speleol. Soc. Bull.
722 16, 71–76.
723 Mottershead, D.N. 1989. Rates and patterns of bedrock denudation by coastal
724 salt spray weathering: a seven-year record. Earth Surf. Process Landforms.
725 14, 383-398.
726 Mustoe, G. E. 1982. The origin of honeycomb weathering. Geol. Soc. Am. Bull.
727 93, 108-115.
728 Mylroie, J.E., Carew, J.L. 1990. The Flank Margin Model for Dissolution Cave
729 Development in Carbonate Platforms: Earth Surf. Process. Land. 15, 413-424.
730 Mylroie J.R, Mylroie J.E. 2007. Development of the carbonate island karst model.
731 J. Cave Karst Stud. 69(1), 59-75.
732 Natalicchio, M., Dela Pierre, F., Lugli, S., Lowenstein, T. K., Feiner, S. J.,
733 Ferrando, S., Manzi, V., Roveri, M. and Clari, P. 2014. Did Late Miocene
734 (Messinian) gypsum precipitate from evaporated marine brines? Insights from
735 the Piedmont Basin (Italy). Geology 42, 179–182.

736 Oerter, E., Singleton, M., Davisson, M. 2018. Hydrogen and oxygen stable
737 isotope dynamics of hyper-saline and salt-saturated aqueous solutions
738 Geochim. Cosmochim. Acta 238, 316-328.
739 Onac, B.P., Wynn, J.G., Sumrall, J.B. 2011. Tracing the sources of cave sulfates:
740 a unique case from Cerna Valley, Romania. Chem. Geol. 288, 105-114.
741 Pierre, C. 2018. The isotopic record of gypsum diagenesis in diluted solutions:
742 Observations in natural salinas and experiments. Chem. Geol. 493, 451-457.
743 Prebble, M.M. 1967. Cavernous weathering in the Taylor Dry Valley, Victoria
744 Land, Antarctica. Nature, 216, 1194-1195.
745 Puch, C, 1998. Grandes Cuevas y simas de España, Barcelona pp. 781-782.
746 Raab, M., Spiro, B., 1991. Sulfur isotopic variations during seawater evaporation
747 with fractional crystallization. Chem. Geol. 86, 323-333.
748 Rodriguez-Navarro, C.E., Doehne, E. 1999. Salt weathering: influence of
749 evaporation rate, supersaturation and crystallization pattern. Earth Surf.
750 Process Landforms 24, 191–209.
751 Sarrazin, P., Chipera, S., Bish, D., Blake, D., Vaniman, D. 2005. Vibrating sample
752 holder for XRD analysis with minimal sample preparation. International Centre
753 for Diffraction Data. Adv. X-ray Anal. 48, 156–164.
754 Sim, M.S., Bosak, T., Ono, S. 2011. Large sulfur isotope fractionation does not
755 require disproportionation. Science 333, 74–77.
756 Sofer, A. 1978. Isotopic composition of hydration water of gypsum. Geochim.
757 Cosmochim. Acta 42, 1141-1149.
758 Van Driessche, A.E.S., Canals, A., Ossorio, M., Reyes, R.C., García-Ruiz, J.M.
759 2016. Unraveling the sulfate sources of (giant) gypsum crystals using gypsum
760 isotope fractionation factors. J. Geol. 124, 235-245.

761 Van Stempvoort, D.R., Krouse, H.R. 1994. Controls of sulfate $\delta^{18}O$: a general
762 model and application to specific environments. In: Alpers, C., Blowes, D.
763 (Eds.), Environmental Geochemistry of Sulfide Oxidation. American Chemical
764 Society Symposium Series, 550, 446–480.

765 Wexler, A., Hasegawa, S. 1954. Relative humidity-temperature relationships of
766 some saturated salt solutions in the temperature range 0°C to 50 °C. J. Res.
767 Natl. Bur. Stand, 53, 19, RP 2512.
768 White, W.B., White, E.L. 2003. Gypsum wedging and cavern breakdown: Studies
769 in the Mammoth Cave System, Kentucky: Journal of Caves and Karst Studies.
770 65, 43–52.
771 Zerkle, A.L., Jones, D.S., Farquhar, J., Macalady J.L. 2016. Sulfur isotope values
772 in the sulfidic Frasassi cave system, central Italy: a case study of a
773 chemolithotrophic S based ecosystem Geochim. Cosmochim. Acta 173, 373-
774 386.
775
776
777
778
779
780
781
782
783
784
785

FIGURES AND TABLES CAPTIONS

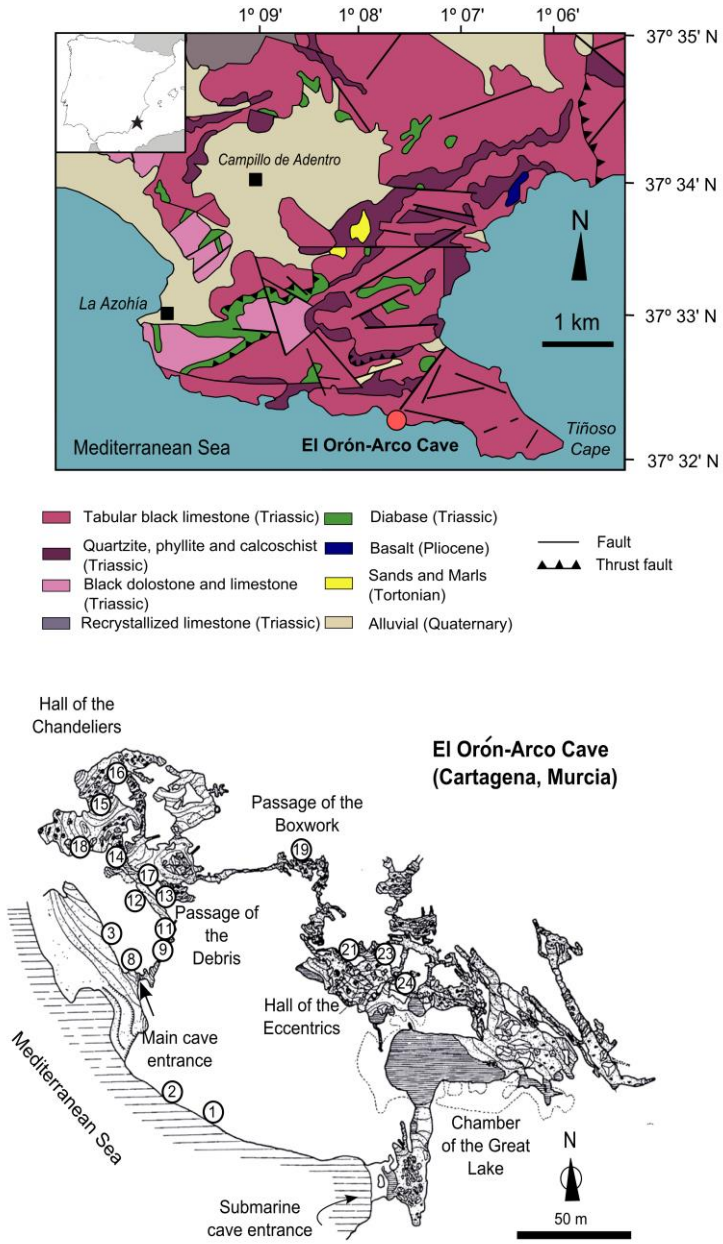

Figure 1. Geological setting of Cabo Tiñoso (after Gordillo *et al.,* 1972) and topography of El Orón-Arco Cave (produced by Llamusí, Inglés and Ros, 1984-1998). Sampling sites are indicated.

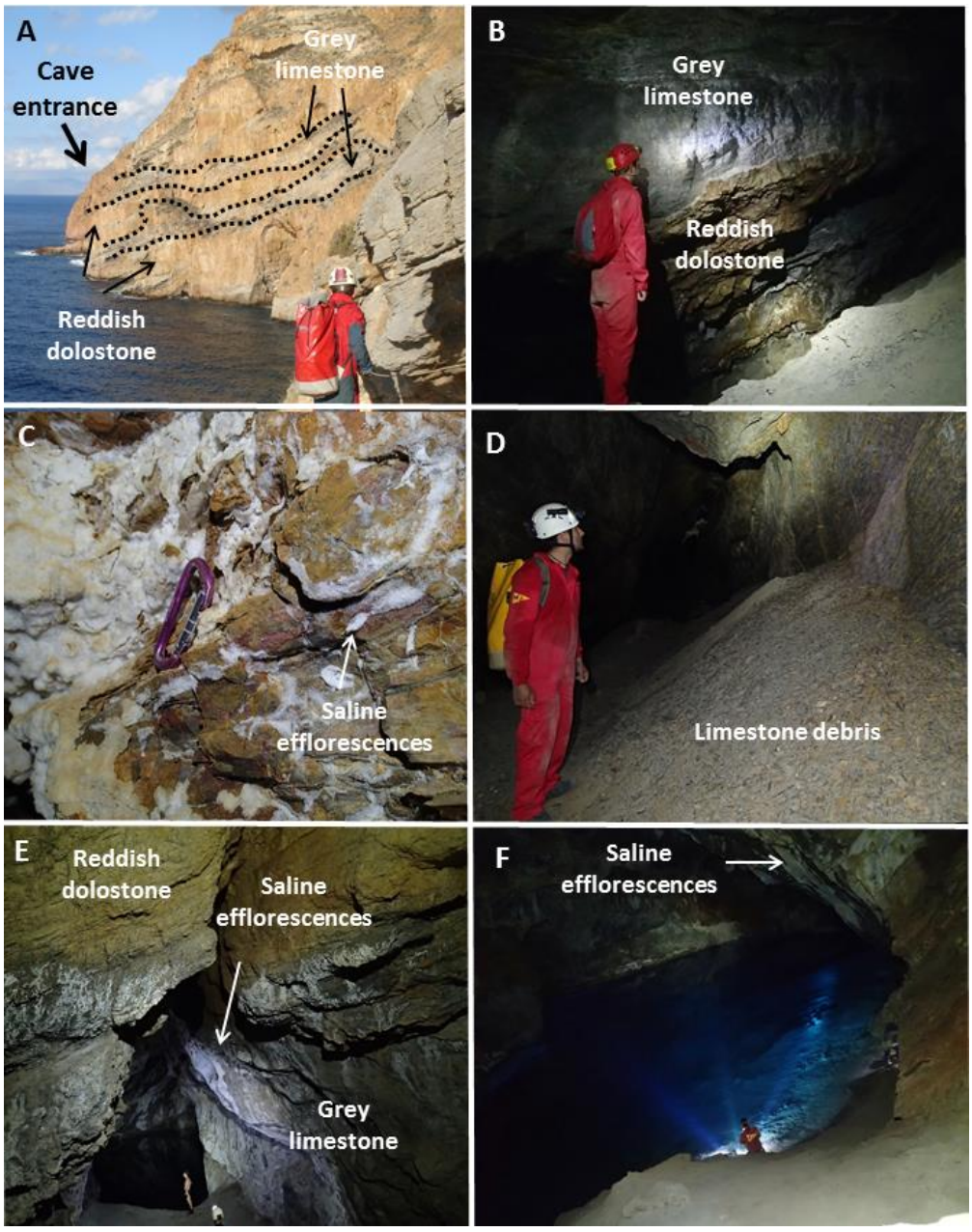

794

795 **Figure 2. A**. Interbedded highly foliated greyish limestones and reddish dolostone
796 in which El Orón-Arco Cave is hosted; **B**. Contact between the limestones and
797 the dolostone inside the cave; **C**. Saline concretions on the cave walls. **D**. Piles
798 of unsorted rock fragments on the cave walls; **E**. Altered limestone and saline
799 concretions; **F**. Saline efflorescences on the walls of the Hall of the Great Lake.

800

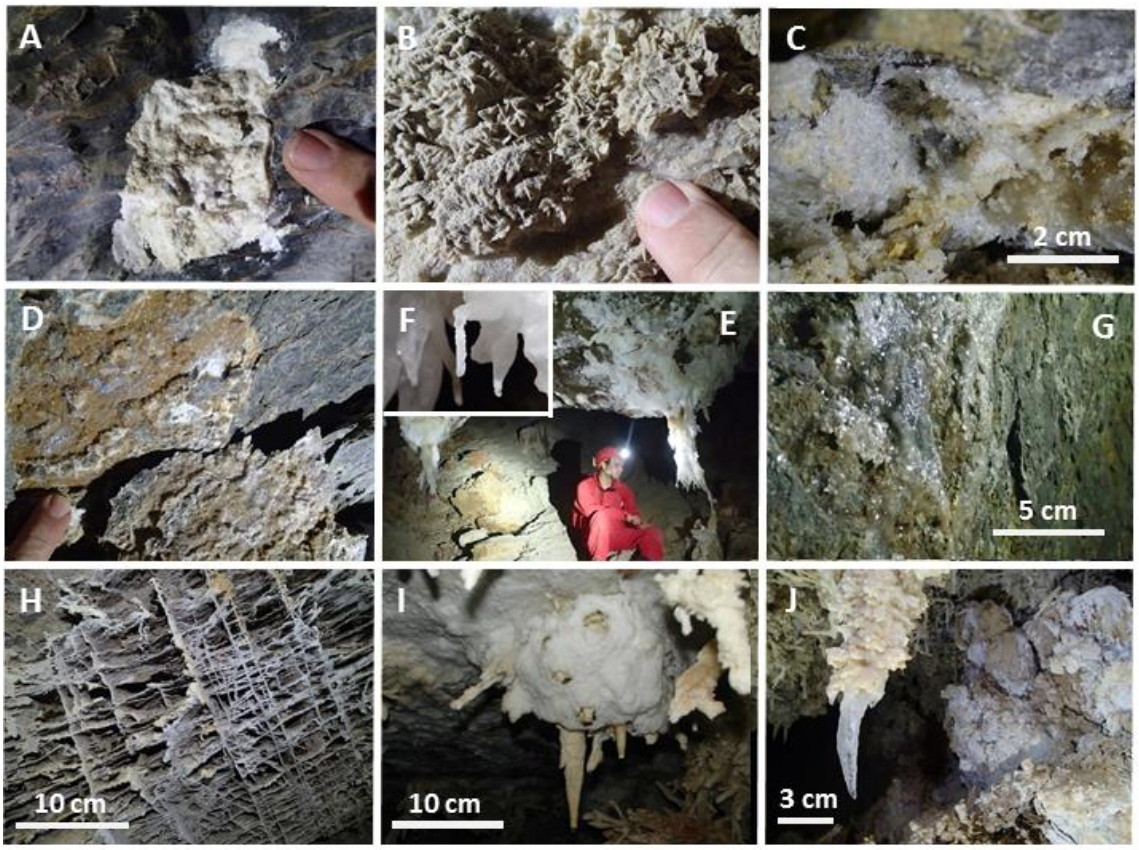

Figure 3. Speleothems in El Orón-Arco Cave: **A**. Concretions of gypsum on the carbonate host-rock; **B**. Aggregate of gypsum crystals covered by sandy materials; **C**. Saline concretions (gypsum + halite) in planes of the host-rock; **D**. Sugar-textured calcite infillings in planes of the host-rock; **E**. Gypsum 'chandeliers'; **F**. Details of the apex of a 'chandelier'; **G**. Saline coating on the cave walls; **H**. Carbonate boxwork formations covered with microcrystalline gypsum; **I**. Hollow gypsum hemispheres ('blisters') surrounded by carbonate eccentrics; **J**. Gypsum single crystals hanging from the tip of a carbonate dripstone.

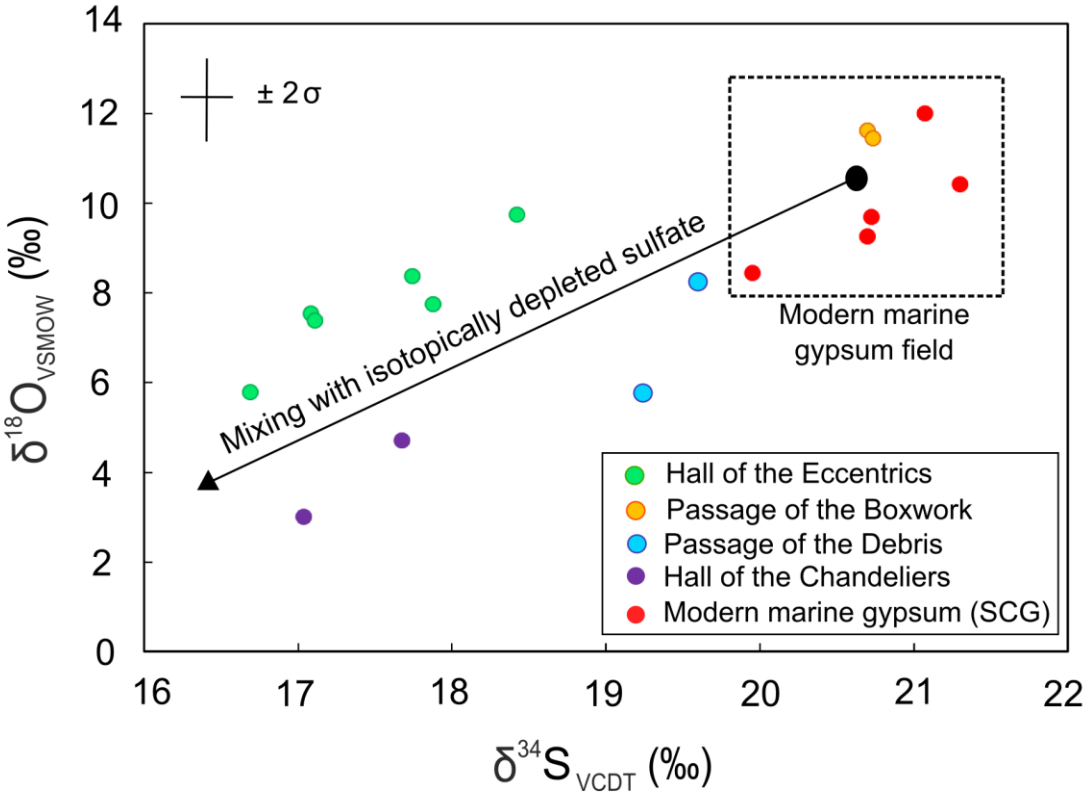

812

813 **Figure 4.** Sulfur and oxygen isotope composition of gypsum speleothems from

814 El Orón-Arco Cave. The $\delta^{34}S$ and $\delta^{18}O_{SO4}$ values of modern marine gypsum (SCG

815 samples) from a nearby salt factory (Salina of Cabo de Gata, Almeria, SE Spain;

816 Evans et al., 2015) are presented for comparison.

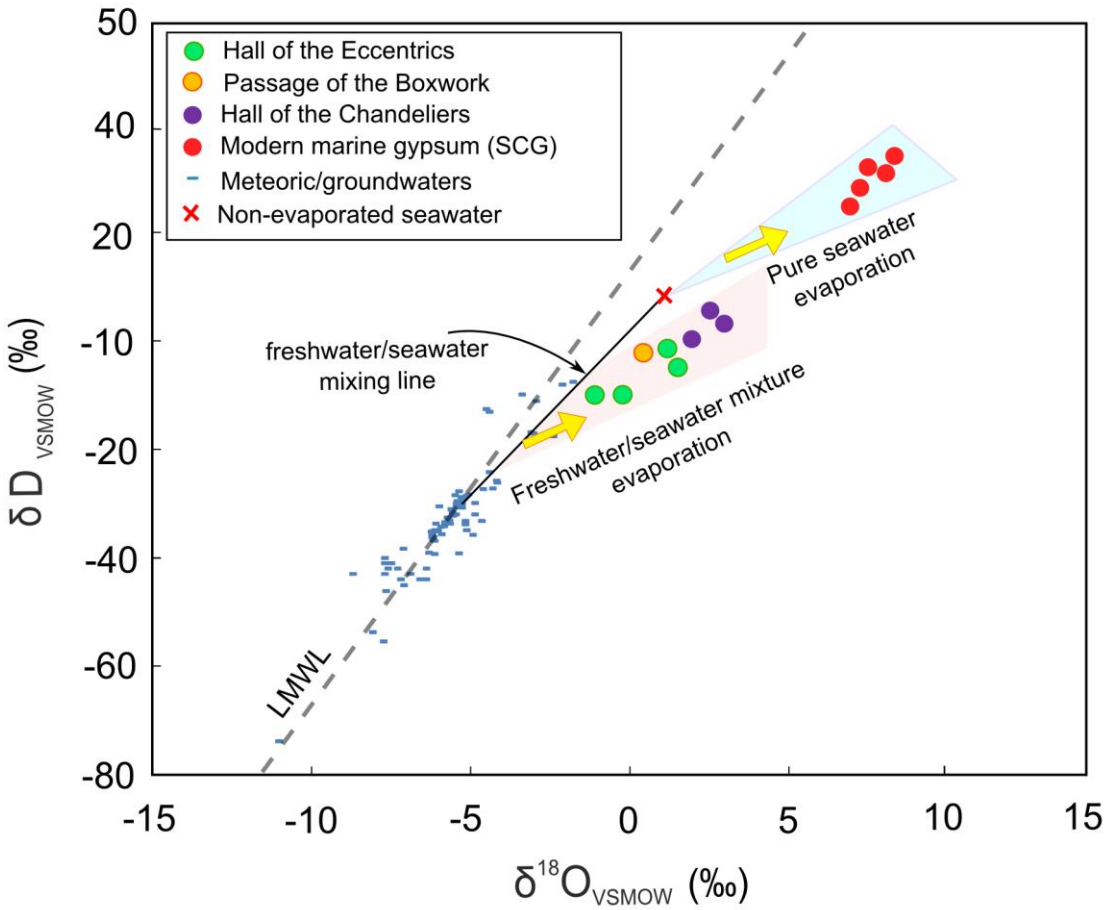

817

818 **Figure 5.** Oxygen and hydrogen isotopes of speleothem-forming water in El
819 Orón-Arco Cave obtained from gypsum hydration water after applying known
820 isotope fractionation factors by Gázquez et al. (2017a) (see main text). Isotope
821 composition of meteoric and groundwaters in SE Spain are given for comparison
822 (Gázquez et al., 2017b), as well as the mother water from which marine gypsum
823 formed in a nearby salt factory (Salina of Cabo de Gata, Almeria, SE Spain;
824 Evans et al., 2015; Gazquez et al., 2017a). Analytical errors are smaller than the
825 symbols.

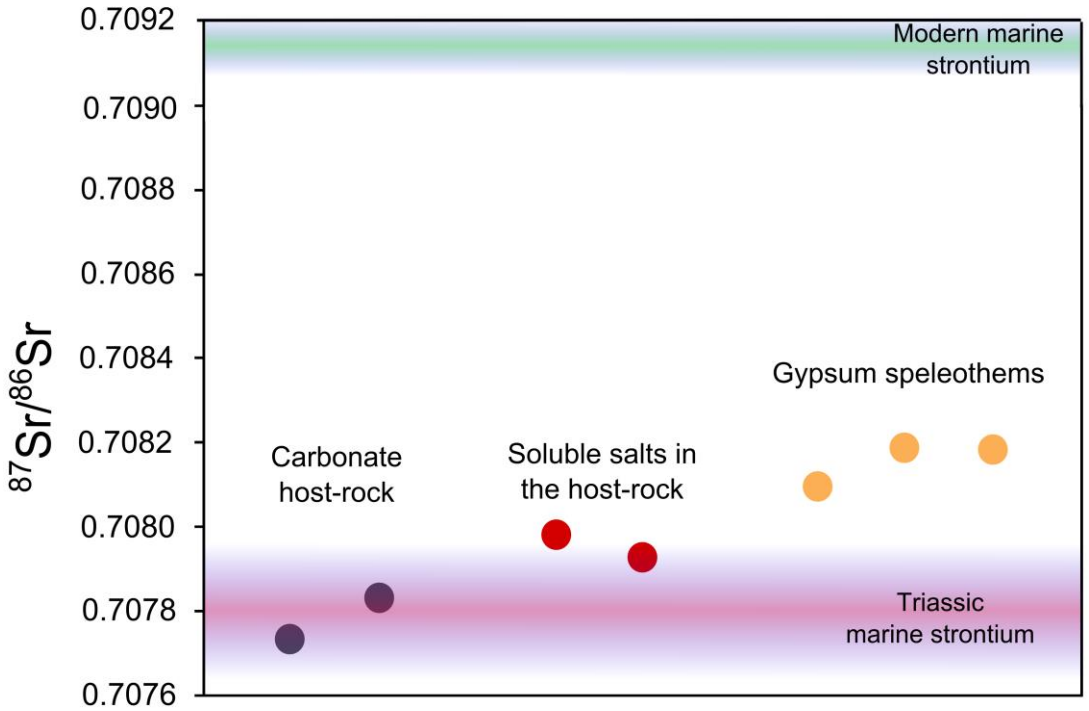

826

827 **Figure 6.** Strontium isotope composition ($^{87}Sr/^{86}Sr$) of gypsum speleothems,
828 carbonate host-rock and soluble salts leached from the host-rock in El Orón-Arco
829 Cave. Analytical errors are smaller than the symbols.

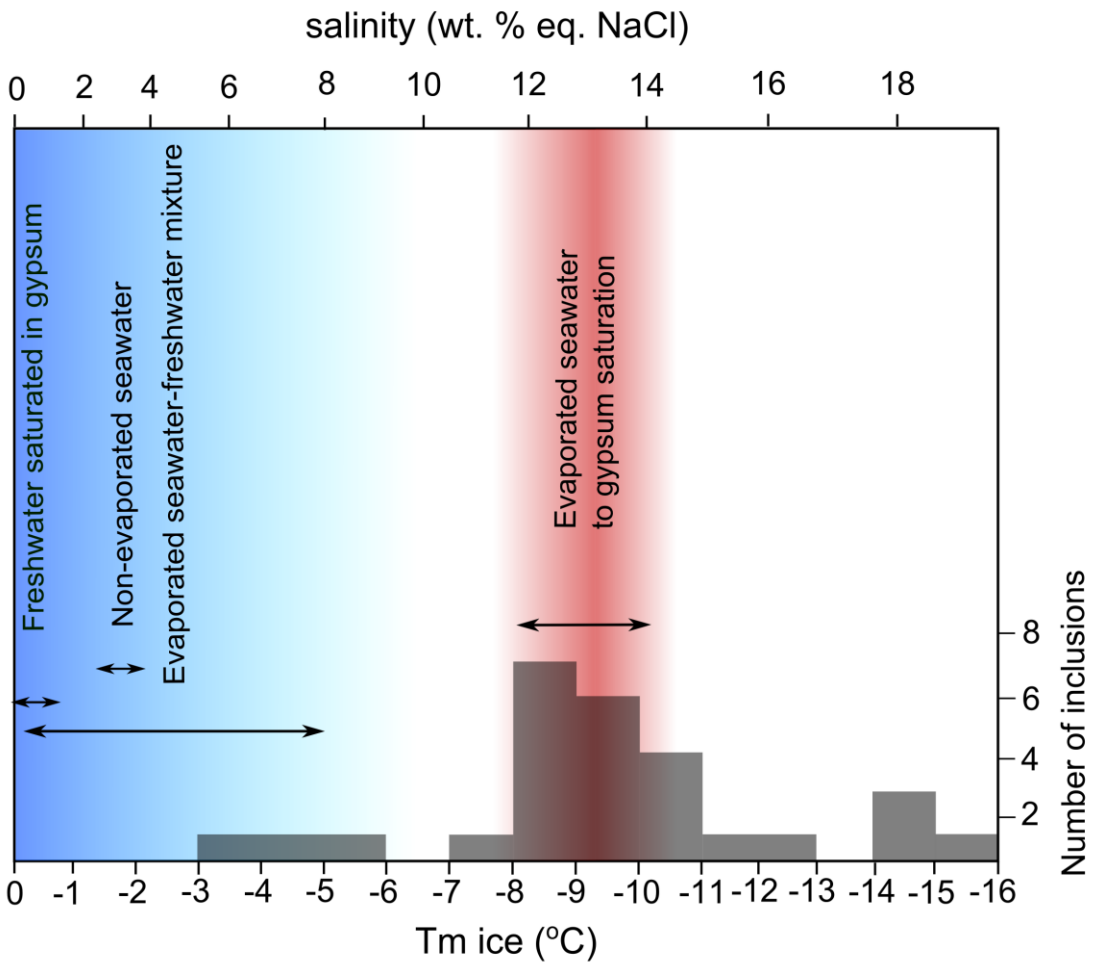

830

831 **Figure 7.** Microthermometry of primary fluid inclusions in gypsum speleothems
832 from El Orón-Arco Cave. Ice melt temperature (T_m) of fluid inclusions were
833 converted to salinity (wt. % eq. NaCl) using the equation of Bodnar (1993).

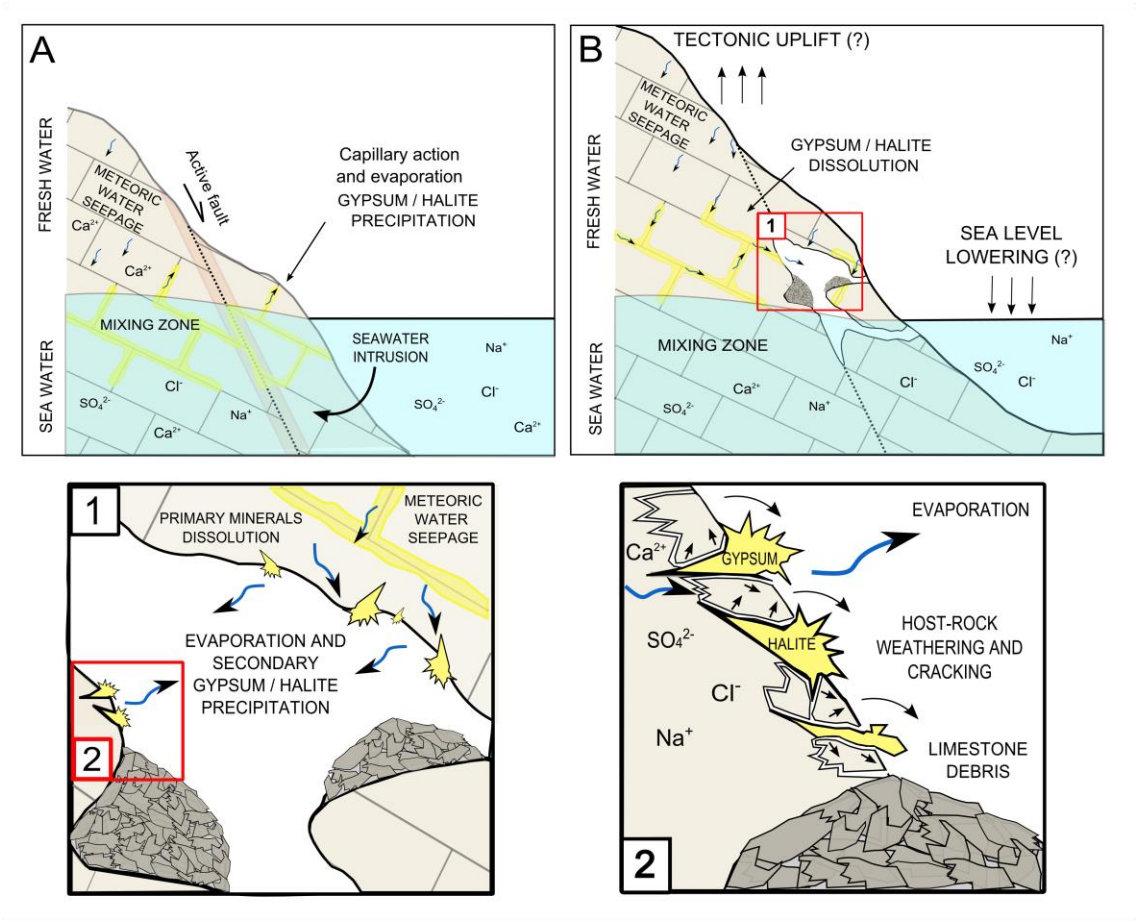

834

835 **Figure 8.** Conceptual sketch of the mechanism that formed El Orón-Arco Cave:
836 **A**. Seawater intrusion and capillary action of brackish water that evaporates in
837 voids of the host-rock, leading to primary evaporites (mostly gypsum and halite)
838 precipitation and carbonate weathering; **B**. Enhanced saline weathering by sea
839 salts precipitation with greater contribution of meteoric water seepage and
840 dissolution of primary evaporites in subaerial conditions, resulting in precipitation
841 of secondary evaporites, host-rock cracking and accumulation of debris detached
842 from the cave walls. Panels 1 and 2 are zooms of panel B, showing the idealized
843 weathering process. Note that faulting and tectonics may have also had a
844 significant role during the formation of the cave and meteoric water flow thought
845 the carbonate host-rock, particularly during its initial genetic stages.

846

Sample	Description	Site	Mineralogy	$\delta^{34}S_{SO4}$	$\delta^{18}O_{SO4}$	$\delta^{18}O_{GHW}$	δD_{GHW}	$\delta^{18}O_{MW}$	δD_{MW}	Th (°C)	% NaCl eq	$^{87}Sr/^{86}Sr$
CT-01	Yellowish calcschist	Outside	Calcite	-	-	-	-	-	-	-	-	
CT-02	Grey host-rock	Outside	Calcite	-	-	-	-	-	-	-	-	
CT-03	Infillings along host-rock strata	Outside	Halite, gypsum (-)	-	-	-	-	-	-	-	-	
CT-08	Grey limestone	Outside	Calcite, dolomite (-)	-	-	-	-	-	-	-	-	0.707737 (0.707988)
CT-09	Whitish coating on host-rock	Entrance passage	Gypsum	17.7	8.4	-	-	-	-	-	-	
CT-11	Gypsum 'rose' in sediment	Entrance passage	Gypsum	19.6	8.3	-	-	-	-	-	-	
CT-12	Sugary texture brownish infillings	Passage of the debris	Calcite, dolomite (-)									
CT-13	Crystalline coatings on the cave wall	Passage of the debris	Gypsum, celestine (-)	19.2	5.8	-	-	-	-	-	-	0.708188
CT-14	Reddish host-rock	Hall of the Chandeliers	Dolomite, goethite (-)									
CT-15A	Microcrystalline coatings over chandeliers	Hall of the Chandeliers	Gypsum	17.0	-	5.5	-16.9	2.2	3.2	-	-	
CT-15B	Gypsum chandelier (1)	Hall of the Chandeliers	Gypsum	17.7	4.7	5.8	-13.6	2.5	1.4	-10.7±2.5	14.2±2.5	0.708183
CT-15C	Halite soda-straw	Hall of the Chandeliers	Halite, celestine (-)	-	-	-	-	-	-	-	-	
CT-16	Gypsum chandelier (2)	Hall of the Chandeliers	Gypsum	17.0	3.0	4.8	-16.9	1.5	-2.0	-	-	
CT-17	Microcrystalline gypsum	Passage of the debris	Gypsum	17.1	7.5	4.3	-21.4	1.0	-6.5	-	-	
CT-18A	Yellowish powder in planes of the host-rock	Hall of the Chandeliers	Halite, gypsum, quartz (-)	17.0	-	-	-	-	-	-	-	
CT-18B	Reddish host-rock	Hall of the Chandeliers	Dolomite, goethite (-)	-	-	-	-	-	-	-	-	0.707835 (0.707926)
CT-18D	Whitish veins in the host-rock	Hall of the Chandeliers	Calcite	-	-	-	-	-	-	-	-	
CT-19A	Whitish coatings on boxwork	Hall of the Boxwork	Gypsum	20.7	11.6	3.4	-18.9	0.1	-4.0	-	-	
CT-19B	Boxwork laminae	Hall of the Boxwork	Dolomite, calcite (-)	-	-	-	-	-	-	-	-	
CT-21B	Stalactite	Hall of the Eccentrics	Aragonite	-	-	-	-	-	-	-	-	
CT-21A	Spar on the tip of a stalactite	Hall of the Eccentrics	Gypsum	16.7	5.8	4.1	-18.8	0.8	-3.9	-9.9±2.4	13.3±2.4	
CT-21C	'Blister' speleothem (1)	Hall of the Eccentrics	Gypsum	17.1	7.4	2.6	-24.8	-0.7	-9.9	-	-	0.708095
CT-23A	Microcrystalline coating over stalactite	Hall of the Eccentrics	Gypsum	18.4	9.8	-	-	-	-	-	-	
CT-23A1	Spar on the tip of a stalactite	Hall of the Eccentrics	Gypsum	-	-	-	-	-	-	-5.3±1.9	8.2±2.6	
CT-23B	Stalactite	Hall of the Eccentrics	Aragonite	-	-	-	-	-	-	-	-	
CT-23C	Stalactite	Hall of the Eccentrics	Aragonite	-	-	-	-	-	-	-	-	
CT-24	'Blister' speleothem (2)	Hall of the Eccentrics	Gypsum	17.9	7.8	2.0	-24.7	-2.3	-9.9	-	-	

Table 1. Mineralogical and geochemical analyses of samples from El Orón-Arco Cave. Results of $\delta^{18}O$ and $\delta^{34}S$ in sulfate, $\delta^{18}O$ and δD in gypsum hydration water (GHW) and strontium isotopes ($^{87}Sr/^{86}Sr$) are presented. $^{87}Sr/^{86}Sr$ in brackets correspond to leaches from the carbonate host-rock. The $\delta^{18}O$ and δD of gypsum mother water (MW) have been reconstructed by applying fractionation factors by Gázquez et al. (2017a). Ice melt temperatures of primary fluid inclusions (Tm) in gypsum speleothems and derived salinities (wt. % NaCl eq.) calculated from the equation of Bodnar (1993), are also given

852